PAPER

Check for updates

Sr-doped LaTiO$_2$N photocatalyst for hydrogen evolution reaction synthesized from perovskite-type La–Ti oxide nanoparticles

Mayu Inose,[a,b] Shuhei Nakakura, [iD] [b] Takashi Hisatomi [iD] *[c] and Kazunari Domen [iD] *[c]

LaTiO$_2$N responds to visible light up to a wavelength of 600 nm and so is a promising water splitting photocatalyst. However, structural defects and reduced titanium species generated in this material during the nitridation process promote the recombination of photoexcited electrons and holes, and so reduce its photocatalytic activity. The present work synthesized a Sr-doped La–Ti oxide *via* flame spray pyrolysis followed by heat treatment, and utilized this oxide as a starting material for the oxynitride. Sr doping promoted the formation of a La–Ti oxide having a perovskite-type structure similar to that of LaTiO$_2$N, whereas heat treatment prior to the nitridation enhanced the crystallinity of the resulting perovskite-type Sr-doped La–Ti oxide. These factors reduced the defect concentration in the LaTiO$_2$N, thereby improving the hydrogen evolution activity of the catalyst threefold. The present study demonstrates a means of suppressing the reduction of metal cations and thereby improving the photocatalytic activity of perovskite-type oxynitrides by controlling the structure and crystallinity of the oxide precursor.

Introduction

Hydrogen has a low environmental impact but a high mass-based energy density, and so has the potential to function as an alternative to fossil fuels, allowing a sustainable society to be realized in the future. In this regard, photocatalytic water splitting driven by solar energy is an ideal process for producing green hydrogen.[1–4] Recently, Al-doped SrTiO$_3$ has exhibited an apparent quantum yield (AQY) of almost unity during overall water splitting under near-ultraviolet light.[5] However, it will be necessary to develop photocatalysts responsive to visible light so as to utilize solar energy more efficiently, whereas SrTiO$_3$ only absorbs ultraviolet light.[6–9] Examples of such materials include (oxy)nitrides and oxysulfides such as LaTiO$_2$N, Ta$_3$N$_5$, SrTaO$_2$N, BaTaO$_2$N and Y$_2$Ti$_2$O$_5$S$_2$.[10–13] Among these, LaTiO$_2$N contains relatively inexpensive and abundant metals and is also a promising water splitting photocatalyst capable of functioning under visible light up to 600 nm.[14–16] Even so, the efficiency of

LaTiO$_2$N when applied to the water splitting reaction must be improved to allow for practical applications.

LaTiO$_2$N photocatalysts are conventionally synthesized by heating La–Ti oxides acting as precursors under a flow of NH$_3$ at temperatures above 850 °C.[14–23] Unfortunately, this process readily generates structural defects and reduces Ti atoms to the Ti^{3+} state to produce recombination centers for excited electrons and holes. The use of appropriate precursor oxides is an important aspect of the synthesis of LaTiO$_2$N photocatalysts, because the particle size, crystal structure and morphology of these oxides directly affect the properties of the product. As an example, Maegli *et al.*[23] synthesized LaTiO$_2$N by nitriding La$_2$Ti$_2$O$_7$ that had been produced using a solid-state method and had particle sizes of more than 1 μm. The formation of highly porous LaTiO$_2$N having a large specific surface area has also been shown to improve the dispersion of cocatalysts, thus increasing the oxygen evolution activity of the material. Wang *et al.*[15] reported that mesoporous single crystals of LaTiO$_2$N with exposed (010) and (101) crystal facets could be obtained by nitriding the Ruddlesden-Popper compound NaLaTiO$_4$. In contrast to LaTiO$_2$N generated conventionally, the resulting material was found to promote overall water splitting and also drove the oxygen evolution reaction efficiently, with an AQY of 65% at 420 ± 20 nm. Various synthesis and processing methods have also been proposed as approaches to improving the water splitting performance of LaTiO$_2$N, including flux-based methods,[17,18,24] doping with

[a]Department of Science and Technology, Graduate School of Medicine, Science and Technology, Shinshu University, 4-17-1, Wakasato, Nagano-shi, Nagano 380-8533, Japan
[b]Ichikawa Research Center, Sumitomo Metal Mining Co., Ltd, 3-18-5, Nakakokubun, Ichikawa, Chiba 272-8588, Japan
[c]Institute for Aqua Regeneration, Shinshu University, 4-17-1, Wakasato, Nagano-shi, Nagano 380-8533, Japan. E-mail: hisatomi@shinshu-u.ac.jp, domen@shinshu-u.ac.jp

various elements,[25–28] etching[29] and post-calcination.[16,30] When synthesized from a precursor with a structure similar to that of perovskite-type $LaTiO_2N$, long-range cation migration is minimized, which suppresses the generation of structural defects such as grain boundaries that act as recombination centers for photogenerated electrons and holes. Recently, the authors synthesized Al-doped $LaTiO_2N$ from La–Ti oxide obtained by flame spray pyrolysis (FSP). Interestingly, the obtained La–Ti oxide exhibited a perovskite structure identical to that of $LaTiO_2N$, thereby minimizing structural changes during nitridation.[31] The hydrogen evolution activity was improved as a result of reducing structural defects associated with structural transformation. However, doping with an excessive amount of Al atoms, which were substituted into Ti sites in the material caused discontinuity in the Ti 3d orbitals forming the conduction band.[32,33] This effect reduced the photocatalytic activity. On this basis, it would be desirable to explore alternative doping strategies that effectively suppress the formation of defects in $LaTiO_2N$.

Similar to the effects of substituting Al into the Ti sites of the La–Ti oxide, doping of low-valence elements into the La sites of this same compound would be expected to stabilize the perovskite-type structure. This substitution would also likely suppress discontinuity of the Ti 3d orbitals comprising the conduction band, thus improving the hydrogen evolution activity of the $LaTiO_2N$. In the present study, a Sr-doped La–Ti oxide synthesized by FSP was used as a starting material to produce $LaTiO_2N$. Sr doping facilitated the formation of the perovskite structure, and preheating before nitridation further improved the crystallinity of the particle surface. By optimizing the conditions used to generate the Sr-doped La–Ti oxide as well as the nitridation conditions employed to synthesize the Sr-doped $LaTiO_2N$, a threefold increase in hydrogen evolution activity was obtained compared with undoped $LaTiO_2N$.

Experimental

Preparation of solutions of La, Ti and Sr organometallics for FSP

In a typical synthesis, lanthanum octanoate ($La(C_7H_{15}COO)_3$; 98%, Mitsuwa Chemicals Co., Ltd) and strontium octanoate ($Sr(C_7H_{15}COO)_2$; 97%, Mitsuwa Chemicals Co., Ltd) were dissolved in 2-ethylhexanoic acid ($CH_3(CH_2)_3CH(C_2H_5)COOH$; 99.0%, Tokyo Chemical Industry Co., Ltd) heated to 50 °C, with stirring. Ethanol (99.5%, Fujifilm Wako Pure Chemical Co.) and titanium(IV) 2-ethylhexanoate ($Ti[OCH_2CH(C_2H_5)(CH_2)_3CH_3]_4$; 96% SantaCruz) were subsequently added to the mixture. Solutions were prepared having Sr/(La + Sr) molar ratios of 0, 0.2, 0.3 or 0.5 while keeping the total concentration of Ti at 0.025 M and the (La + Sr)/Ti molar ratio at 1.0. All chemicals were used as received without further purification.

Synthesis of Sr-doped La–Ti oxides and oxynitrides

Sr-doped La–Ti oxides were synthesized by FSP under the same conditions as used in previously reported work, except that a feed rate of 4.0 g min^{-1} was employed.[31] The materials made by this process (each comprising a mass of several grams) were collected on a bag filter, then transferred into alumina crucibles and heated at 900–1100 °C for 3 h in air to obtain crystalline La–Ti oxides. This process is referred to herein as preheating. Each La–Ti oxide was subsequently heated at 700–1000 °C for 15 h under a 200 mL min^{-1} flow of NH_3. The product was washed several times each with 0.1 M HCl and deionized water and then dried by heating at 40 °C under vacuum. This process also removed various by-products. The samples synthesized by the FSP, preheating and nitriding were denoted as LTOX, LTOX-YP and LTONX-YP-ZN, where X, Y, and Z represent the Sr content in atomic percent to the Ti-site, preheating temperature in degree Celsius, and nitridation temperature degree Celsius, respectively. The samples without preheating were denoted as LTONX-ZN.

Cocatalyst loading

A 120 mg quantity of the Sr-doped La–Ti oxynitride was dispersed in water (15 mL) followed by the addition of 0.6 mL of an aqueous solution of $IrCl_3 \cdot nH_2O$ (2 mg mL^{-1} as Ir). This mixture was then heated in a microwave reactor (Monowave 200, Anton Paar) at 150 °C for 10 min. The product was subsequently recovered by filtration and then dried at 40 °C under vacuum. Ru species were additionally loaded using a conventional impregnation-thermal reduction technique. In this process, a portion (0.12 mL) of an aqueous solution of $RuCl_3 \cdot 3H_2O$ (10 mg mL^{-1} as Ru) was added to the specimen, after which the water was evaporated. The recovered sample was heated at 250 °C for 1 h under a mixed H_2/N_2 flow (20/200 mL min^{-1}) to give Ru(1 wt%)/IrO$_x$(1 wt%)/Sr-doped $LaTiO_2N$, where the loading amounts refer to the metal concentrations.

Characterization

The crystal phases were examined by X-ray diffraction (XRD) using a MiniFlex 300 (Rigaku Co., Tokyo, Japan) with Cu Kα radiation, operating at 30 kV and 10 mA. The optical properties of the specimens were assessed using UV-visible diffuse reflectance spectroscopy (DRS; V-670, JASCO Co., Tokyo, Japan) employing an integrating sphere. The bulk compositions of the samples were determined by inductively coupled plasma-optical emission spectroscopy (ICPE-9800, Shimadzu Co., Kyoto, Japan) to determine La, Ti and Al concentrations or the inert gas melting method with an oxygen/nitrogen elemental analyzer (ON836; LECO Co., Michigan, USA) to ascertain O and N concentrations. Valencies and surface compositions were determined by X-ray photoelectron spectroscopy (XPS; Versa Probe I, Ulvac-phi, Inc., Kanagawa, Japan). The binding energy was calibrated using the C 1s peak (284.6 eV). The Ti 2p spectra acquired in this manner were deconvoluted assuming Ti^{3+} and Ti^{4+} peaks. The particles size and shapes were observed by scanning electron microscopy (SEM; SU8000, Hitachi High-Tech Co., Tokyo, Japan). Particle morphologies were investigated by corrector-spherical aberration scanning transmission electron microscopy (Cs-TEM; JEM-ARM-200F,

200 kV, JEOL Ltd, Tokyo, Japan) using the high-angle annular dark field (HAADF) mode. Atomic ratios were determined using Cs-TEM coupled with energy dispersive X-ray spectroscopy (EDX; JED-2300T, JEOL Ltd, Tokyo, Japan).

Photocatalytic reactions

Photocatalytic hydrogen evolution reactions were carried out in a Pyrex reaction vessel connected to a closed gas circulation system. In a typical experiment, a quantity of the Ru/IrO$_x$-loaded photocatalyst (100 mg) was dispersed in 100 mL of an aqueous methanol solution (13 vol%), in which the methanol functioned as a sacrificial electron donor. After complete removal of air from the suspension by evacuation, Ar was added to the reaction system to a pressure of 10 kPa. The suspension was subsequently cooled to 15 °C by circulating cooling water and then irradiated with visible light ($\lambda >$ 420 nm) from a 300 W Xe lamp equipped with a dichroic mirror and an L42 cut-off filter. The gaseous reaction products were analyzed by a gas chromatography system that was integrated into the closed circulation system and consisted of a gas chromatograph (GC-8A; Shimadzu) equipped with 5 Å molecular sieve columns and a thermal conductivity detector, using Ar as the carrier gas.

AQY assessments

The AQY values associated with the hydrogen evolution reactions over the various specimens were determined under the same experimental conditions described above expect for the use of a 300 W Xe lamp (MAX-303, Asahi Spectra, Japan) equipped with a 420 nm bandpass filter as a light source. The AQY values were calculated as

$$AQY\,(\%) = \frac{2 \times n(\mathrm{H_2})}{n(\mathrm{photons})} \times 100, \tag{1}$$

where $n(\mathrm{H_2})$ and $n(\mathrm{photons})$ are the quantities of evolved H_2 molecules and incident photons, respectively. The latter value was determined with a grating spectroradiometer (LS-100; EKO Instruments Co., Ltd, Japan).

Results and discussion

La–Ti oxides and LaTiO$_2$N synthesized with various Sr contents

Fig. 1A shows the XRD patterns for La–Ti oxides having various Sr concentrations synthesized by FSP. Although each material generated broad peaks, each pattern indicates a simple perovskite-type structure similar to that of LaTiO$_3$ (ICDD: 01-070-2293) as the major component, together with La$_2$Ti$_2$O$_7$ (ICDD: 01-081-1066) as a minor product. The La$_2$Ti$_2$O$_7$ phase almost disappeared at a Sr doping level of 20 mol%, similar to the effects seen in trials with Al doping.[31] The formation of a simple perovskite-type structure was evidently promoted with increasing extent of Sr doping because the Ti-deficient LaTiO$_3$ and SrTiO$_3$ could form a solid solution and maintain charge neutrality. Fig. 1B presents the XRD pat-

terns for the La–Ti oxides after preheating at 1000 °C for 3 h. In the case of the undoped La–Ti oxide, the thermodynamically stable compound La$_2$Ti$_2$O$_7$ was formed (Fig. 1B (e)). In contrast, the Sr-doped La–Ti oxides (Fig. 1B(f) and (g)) partly maintained a simple perovskite-type, with the material containing 50 mol% Sr having primarily this structure (Fig. 1B (h)). Evidently, Sr doping stabilized the perovskite-type structure of the original La–Ti oxide. Following nitridation, peaks attributable to a LaTiO$_2$N phase (ICDD: 01-079-2293) were observed, together with a peak at approximately 31° attributed to La$_2$O$_3$ (Fig. S1). Following the acid treatment, a single LaTiO$_2$N phase was present (Fig. 1C). This observation indicates that perovskite-type La–Ti oxide containing Ti deficiency forms LaTiO$_2$N without Ti deficiency, with minimal structural changes, through cation rearrangement while preserving the perovskite framework. The XRD peaks associated with the LaTiO$_2$N phase were found to appear at higher angles, closer to those for SrTiO$_3$ (ICDD: 01-090-2457), with increasing Sr content (Fig. S2). These results suggest that Sr atoms were substituted into La sites within the LaTiO$_2$N crystal lattice, considering their ionic radii. The results shown in Fig. S3 and Table S1 demonstrate that the Sr/(La + Sr) ratio in the particles was almost the same as that in the original mixture of raw materials, providing further evidence that Sr was truly doped into the material.

Fig. 1D shows DRS data for LaTiO$_2$N samples doped with various amounts of Sr and nitrided at 900 °C for 15 h, produced with and without the preheating step. The absorption edge for each material was approximately 580 nm regardless of the Sr content. In previous work with Al-doped LaTiO$_2$N by the authors,[31] the substitution of Al atoms at Ti sites was found to widen the band gap appreciably because the density of the Ti 3d orbitals forming the conduction band minimum was decreased. In the present study, the doping of Sr atoms into La sites did not greatly affect the band gap energy level because the La orbitals were not associated with the formation of the conduction band.[34] As the Sr content was increased, the absorption at wavelengths longer than the absorption edge for LaTiO$_2$N (that is, >670 nm) became weaker regardless of whether preheating was applied or not. However, as shown Fig. 1D(i)–(l), preheating further reduced this absorption compared with the absence of preheating (Fig. 1D(i′)–(l′)), suggesting a reduction in the defect density. In addition, it was found that the proportion of Ti^{3+} was reduced by Sr doping (Fig. S4). The Ti binding energy for each sample was in the range of 456–457 eV, consistent with the values reported in the literature. The Ti 2p spectra could be deconvoluted into peaks related to Ti^{3+} and Ti^{4+} species.[14,26,35–38] This observation is further supported by the increase in the formal valence of Ti upon Sr doping, as shown in Table S2. It is possible that the suppression of Ti^{3+} reduction through Sr doping contributed to the enhancement of hydrogen evolution activity.

The Sr-doped LaTiO$_2$N samples were found to evolve hydrogen from aqueous methanol solutions under visible light irradiation after a cocatalyst was loaded, as shown in Fig. 1E.
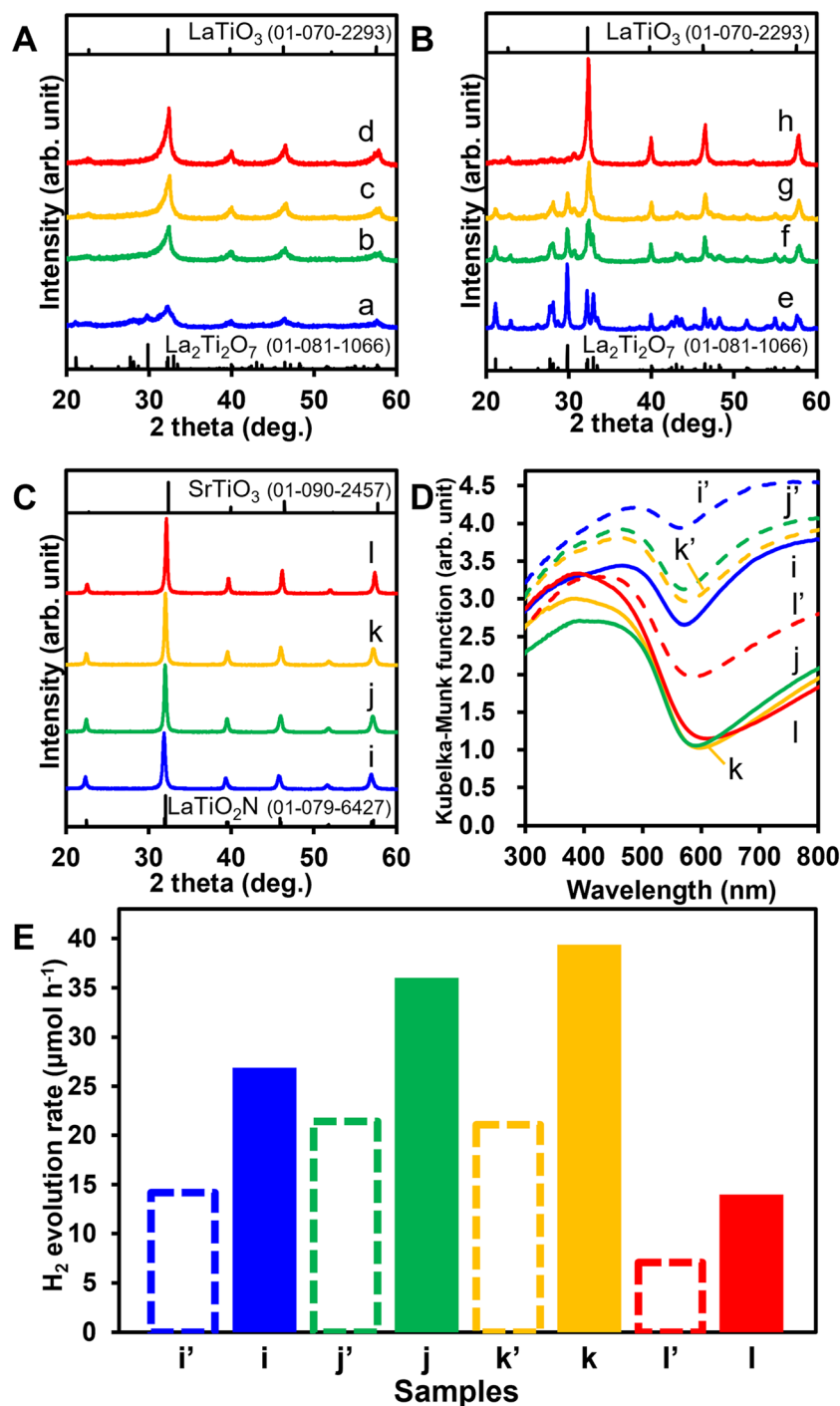
Fig. 1 Characterization and evaluation of La–Ti oxide and LaTiO$_2$N specimens with various Sr contents. XRD patterns for La–Ti oxides after (A) synthesis by FSP, (B) preheating, and (C) nitridation and acid-treatment to produce LaTiO$_2$N. (D) DRS data obtained from LaTiO$_2$N specimens produced with and without preheating. (E) The hydrogen evolution rates for LaTiO$_2$N specimens under visible light (λ > 420 nm) generated by a Xe lamp. Reaction conditions: 100 mg photocatalyst (Ru(1 wt%)/IrO$_x$(1 wt%)/LaTiO$_2$N:Sr); 100 mL of a 15 vol% methanol aqueous solution. Samples: (a) LTO0, (b) LTO20, (c) LTO30, (d) LTO50, (e) LTO0-1000P, (f) LTO20-1000P, (g) LTO30-1000P, (h) LTO50-1000P, (i) LTON0-1000P-900N, (j) LTON20-1000P-900N, (k)LTON30-1000P-900N, (l) LTON50-1000P-900N, (i') LTON0-900N, (j') LTON20-900N, (k') LTON30-900N, and (l') LTON50-900N.

The incorporation of Sr at 20 and 30 mol% evidently increased the hydrogen evolution activity (Fig. 1E(i')–(k')), attributable to the decreased structural defects resulting from the increased proportion of perovskite-type La–Ti oxide formed by FSP and

Sr doping. From the results in Fig. 1E(i)–(l) it is apparent that the hydrogen evolution activities of Sr-doped LaTiO$_2$N specimens made with preheating were approximately twice those obtained from materials that were not preheated (Fig. 1E(i')–

(l′)). The LTON30-1000P-900N showed the highest hydrogen evolution activity (Fig. 1E(k)), and this increased activity is ascribed to the formation of a perovskite-type La–Ti oxide having a low concentration of defects. It is evident that both the incorporation of Sr and the preheating step inhibited the discontinuity of Ti 3d orbitals, unlike the doping of Al atoms into Ti sites. Even so, the hydrogen evolution activity of the LTON50-1000P-900N was decreased (Fig. 1E(l′)). This effect likely occurred because an overly high Sr concentration in the material resulted in a reduced N content so as to maintain charge neutrality (Table S2). The valence band maximum for LaTiO$_2$N is composed of hybridized O and N 2p orbitals. Hence, a decreased proportion of N would be expected to inhibit the migration of holes. This effect would take place even though the extent of deviation from the stoichiometry of Sr-doped LaTiO$_2$N (that is, the N deficient formula La$_{1-x}$Sr$_x$TiO$_{2+x}$N$_{1-x}$) would be reduced with increasing the Sr content. A similar trend was observed in previous work with Al-doped LaTiO$_2$N by the authors.[31]

Effect of the preheating of Sr-doped La–Ti oxides and Sr-doped LaTiO$_2$N

The LTON30-1100P-900N exhibited the highest hydrogen evolution activity (Fig. S5), together with the lowest absorption at wavelengths longer than the absorption edge (Fig. S6). Accordingly, the effects of preheating at this temperature on the physical properties of both the 30 mol% Sr-doped La–Ti oxide and the corresponding oxynitride were investigated. Fig. 2A–D show HAADF images and selected-area electron diffraction patterns acquired with ⟨111⟩ incidence from perovskite-type LTO30 (Fig. 2A and B) and LTO30-1100P (Fig. 2C and D). Heavier atoms generate brighter regions in HAADF images, and so the bright spots in these images indicate the positions of La and Ti atoms. Along the ⟨111⟩ direction the perovskite-type La–Ti oxide, La and Ti atoms overlapped to form hexahedral atomic arrangements. As shown in Fig. 2A, the regular arrangement of atoms originally observed inside a particle became disordered close to the particle surface, and the particle shape was rounded. The particle surface also appears to have been covered by an amorphous layer or by layered structures (indicated by the yellow arrow), for which further evidence is provided by the selected-area electron diffraction patterns (Fig. 2B). In contrast, the particles after preheating exhibited exposed facets attributable to {111} planes on the particle surfaces (Fig. 2C). Diffraction spots are also clearly visible in Fig. 2D along with linear streaks that may reflect the layered structure indicated by the yellow arrow in Fig. 2C. Fig. 2E provides a magnified view of the layered structure seen in Fig. 2C. The interatomic spacing for this structure was d = 2.57 Å, in agreement with the interatomic spacing for the (005) planes of L$_2$Ti$_2$O$_7$. In accordance with these observations, Fig. S7 demonstrates that the La$_2$Ti$_2$O$_7$ XRD peak became more intense as the preheating temperature was increased. On the other hand, the XPS results (Fig. S4B) indicate that preheating did not affect the proportion of Ti^{3+} on the surfaces of the LaTiO$_2$N particles. It should also be noted that the pro-

portion of Ti^{3+} species in each material could have been over-estimated because the chemical shift resulting from the replacement of O with the less electronegative element N was not taken into consideration. From the above results, it is considered that the preheating step promoted crystallization of the La–Ti oxide while suppressing the loss of the Sr dopant. As a result, the concentration of defects in the LaTiO$_2$N was decreased (Fig. 1D) and the hydrogen evolution activity improved.

The effect of preheating at various temperatures on the particle sizes in the Sr-doped La–Ti oxide and LaTiO$_2$N was also investigated. The LTO30 (Fig. S8) consisted of fine particles less than 20 nm in size. The organometallic salts were initially vaporized in the flame and subsequently nucleated, such that growth occurred through coagulation and coalescence during rapid quenching. After nitridation, the Sr-doped LaTiO$_2$N particles made without preheating had a size of approximately 50 nm (Fig. S9), meaning that the particle size was more than doubled. Fig. 3 show SEM images of 30 mol% Sr-doped samples before and after nitridation with preheating. The particles sizes in both the Sr-doped La–Ti oxide and oxynitride increased with increases in the preheating temperature. Clearly, the particle sizes in the Sr-doped La–Ti oxide and in the resulting oxynitride were correlated. Furthermore, the increase in particle size during nitridation to give LaTiO$_2$N was smaller with preheating than without. As shown in Fig. 3F, the particles size in the LTO30-1100P-900N was approximately 200 nm. In addition, several pores (indicated with yellow arrows) were found to have formed on the particle surfaces. This effect was caused by contraction of the material during the nitridation of the layered La$_2$Ti$_2$O$_7$ phase on the surface of the La–Ti oxide.[38]

As shown in Fig. S5, the hydrogen evolution activity for the Sr-doped LaTiO$_2$N was improved with increasing preheating temperature. Upon increasing this temperature from 900 to 1000 °C, the activity was increased by a factor of 1.7, primarily because the higher temperature reduced the defect concentration in the material (Fig. S6). However, when the preheating temperature was raised from 1000 to 1100 °C, only a marginal improvement in activity was observed. Hence, it is possible that a La$_2$Ti$_2$O$_7$ phase was formed more readily at higher temperatures.

Effect of the nitridation temperature

Preheating decreased the concentration of defects in the Sr-doped LaTiO$_2$N even though the proportion of Ti^{3+} in the material was not changed. This led to an increase in hydrogen evolution activity. To suppress the reduction of Ti^{4+}, the nitridation of the precursor subjected to preheating at 1100 °C was conducted at lower temperatures. Fig. 4A presents the XRD patterns for the LTO30-1100P (Fig. 4A(a)) and LaTiO$_2$N nitrided at various temperatures and treated with acid (Fig. 4A(b)–(e)). The sample after nitridation at 700 °C remained similar to the original oxide and contained the La$_2$Ti$_2$O$_7$ phase, whereas single-phase LaTiO$_2$N was obtained at nitridation temperatures above 800 °C. In the case that undoped La$_2$Ti$_2$O$_7$ was
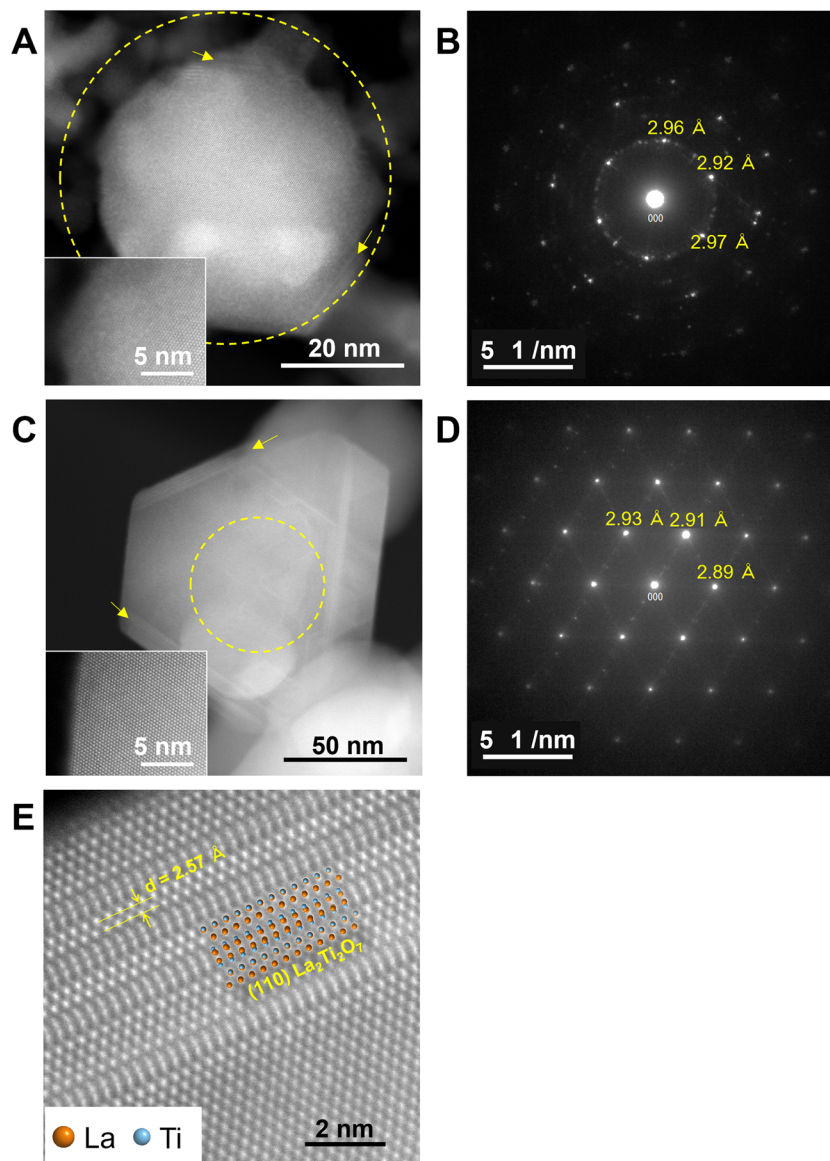
Fig. 2 TEM analysis of the $LaTiO_3$ phase observed along the $\langle 111 \rangle$ direction in a La–Ti oxide (A and B) LTO30 and (C and D) LTO30-1100P. (A and C) HAADF images and (B and D) selected-area electron diffraction patterns for the $LaTiO_3$ phase observed along the $\langle 111 \rangle$ direction within the regions indicated by the yellow circles in (A) and (C), respectively. (E) A magnified image of the layered structure shown in (C). The La and Ti atoms in the $La_2Ti_2O_7$ (110) plane are indicated by yellow and light blue spheres, respectively.

nitrided at 800 °C, some unreacted $La_2Ti_2O_7$ remained (Fig. S10). These results reflect the increased capacity of the Sr-doped La–Ti oxide to generate the $LaTiO_2N$ phase as a consequence of the similar crystal structures of the materials. The full width at half maximum for the peak related to the 121 diffraction for the Sr-doped $LaTiO_2N$ specimens nitrided at 800, 900 and 1000 °C was 0.40°, 0.34° and 0.29°, respectively. The absorption edge for the Sr-doped $LaTiO_2N$ samples processed at 800 °C and above was approximately 580 nm, as can be seen in Fig. 4B(c)–(e). In contrast, as shown in Fig. 4B(b), the sample obtained *via* nitridation at 700 °C had a shorter absorption edge wavelength and weaker visible light absorption, both stemming from insufficient nitridation.[22,39] Fig. 4C

shows the Ti 2p XPS spectra for 30 mol% Sr-doped $LaTiO_2N$ specimens obtained by nitridation at temperatures of 700 to 1000 °C. The proportion of Ti^{3+} species on the surfaces of these materials evidently decreased with decreasing nitridation temperature from 900 to 700 °C. The formation of Ti^{3+} species resulting from anion defects was also confirmed by the absorption seen at about 800 nm in the DRS data (Fig. 4B).[23,38,39] These absorption values were consistent with the Ti^{3+} proportions estimated from the XPS results.

Fig. 4D summarizes the hydrogen evolution rates observed using 30 mol% Sr-doped $LaTiO_2N$ samples synthesized at various nitridation temperatures. The hydrogen evolution activity of the LTO30-1100P-700N was lower than the LTO30-
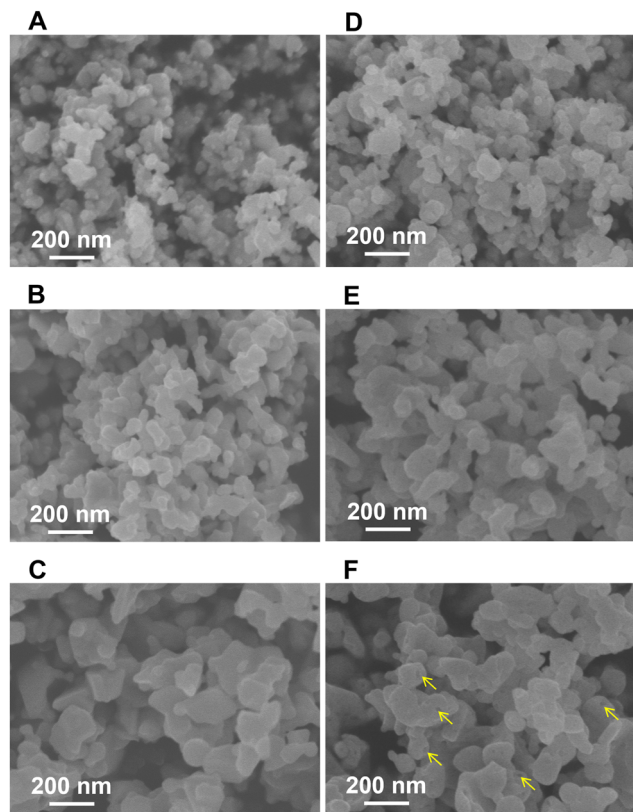
Fig. 3 SEM images of (A) LTO30-900P, (B) LTO30-1000P, (C) LTO30-1100P, (D) LTON30-900P-900N, (E) LTON30-1000P-900N, and (F) LTO30-1100P-900N.

Fig. 4 Properties of 30 mol% Sr-doped LaTiO$_2$N specimens prepared by nitriding oxides preheated at 1100 °C, employing various nitridation temperatures. (A) XRD patterns, (B) DRS data, (C) Ti 2p XPS spectra, and (D) hydrogen evolution rates obtained from the (a) LTO30-1100P, (b) LTON30-1100P-700N, (c) LTON30–1100P-800N, (d) LTON30-1100P-900N or (e) LTON30-1100P-1000N. Reaction conditions for (D): 100 mg of photocatalyst (Ru(1 wt%)/IrO$_x$(1 wt%)/LaTiO$_2$N:Sr); 100 mL of a 15 vol% methanol aqueous solution; visible light (λ > 420 nm) irradiation from a Xe lamp.

1100P-800N specimen because of the limited nitridation of the former. Despite the decreased Ti^{3+} concentration in the LTO30-1100P-800N, this sample showed almost the same hydrogen evolution activity as that for the LTO30-1100P-900N. Because the former exhibited a larger full width at half maximum, this result is attributed to the trade-off between increases in the degree of crystallinity of the LaTiO$_2$N phase and increases in the concentration of Ti^{3+} species at higher nitridation temperatures. Compared with the material undergoing nitridation at 900 °C, the hydrogen evolution activity for the 30 mol% Sr-doped LaTiO$_2$N nitrided at 1000 °C was decreased, even though the proportion of Ti^{3+} was not changed and the full width at half maximum for the latter was smaller. Further investigations are needed to determine why the activity of the catalyst was lowered despite the improved crystallinity.

The hydrogen evolution rate for the 30 mol% Sr-doped LaTiO$_2$N generated with preheating at 1100 °C was increased threefold compared with the undoped LaTiO$_2$N produced without preheating. To evaluate the stability of the photocatalyst, a hydrogen evolution cycling test were carried out using LTON30-1100P-800N (Fig. S11). Although the hydrogen evolution activity decreased from the first to the second cycle, the XRD patterns before and after the reaction showed no sig-
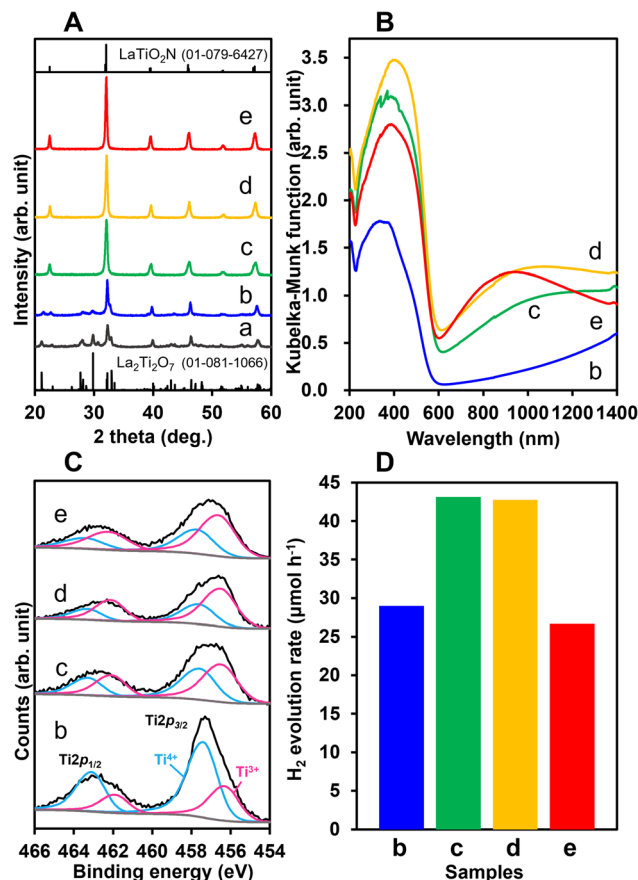
nificant changes (Fig. S12). In addition, the hydrogen evolution activity remained almost unchanged between the second and third cycles, demonstrating reasonable stability of the photocatalyst. The AQY for the LTO30-1100P-800N was determined to be 0.24%. Li *et al.* previously synthesized LaTiO$_2$N at an even lower temperature of 700 °C using hollow, spherical La–Ti oxide particles as a precursor, and reported a quantum efficiency of 3.4% in the hydrogen evolution reaction.[40] The optimum nitridation temperature for LaTiO$_2$N appears to vary depending on the type of oxide precursor that is employed. Further optimization of the dopant type and amount as well as the particle size in the oxide precursor, and ensuring that nitridation occurs while maintaining the perovskite structure, is expected to further improve the hydrogen evolution activity of such materials. These results demonstrate that perovskite-type La–Ti oxides facilitate the synthesis of LaTiO$_2$N under milder nitriding conditions, thereby suppressing the generation of Ti^{3+}.

Conclusion

The effects of the conditions used to prepare and nitride Sr-doped La–Ti oxides synthesized by FSP were investigated, with the aim of improving the hydrogen evolution activity of LaTiO$_2$N by suppressing defect formation. Sr doping improved the thermodynamic stability of the perovskite-type La–Ti oxide and promoted the formation of LaTiO$_2$N at low temperatures. Furthermore, the perovskite structure of the original La–Ti oxide was maintained after preheating, and round particles having amorphous surface layers acquired crystalline surface and facets. These factors reduced the defect concentration in the bulk LaTiO$_2$N, leading to higher hydrogen evolution activity compared with undoped LaTiO$_2$N. In contrast, an undoped perovskite-type La–Ti oxide synthesized by FSP transformed to La$_2$Ti$_2$O$_7$ during the preheating step and did not undergo sufficient nitridation at low temperatures. Sr-doped LaTiO$_2$N showed the highest hydrogen evolution activity in conjunction with a Sr content of 30 mol%. Higher Sr levels resulted in a decreased concentration of N in the material that, in turn, inhibited the migration of holes and reduced the performance of the catalyst.

The present study demonstrates that preheating can reduce the density of defects in such materials to enhance photocatalytic activity, and also provides insights into the importance of the crystallinity and structure of the oxide precursor. Sr-doped LaTiO$_2$N nitrided at a relatively low temperature of 800 °C exhibited high activity based on inhibiting the reduction of metal cations in the oxynitride, despite the somewhat lower crystallinity of the product. Enhancing the degree of crystallization of the oxynitride at low temperatures will likely further enhance the photocatalytic activity of this compound.

Conflicts of interest

The authors declare the following competing financial interests: M. I., S. N., T. H. and K. D. hold Japanese Unexamined Patent Applications related to this work.

Data availability

The data supporting this article have been included as part of the supplementary information (SI). Supplementary information is available. See DOI: https://doi.org/10.1039/d5dt01621e.

References

1 S. Ahmad, A. Ullah, A. Samreen, M. Qasim, K. Nawaz, W. Ahmad, A. Alnaser, A. M. Kannan and M. Egilmez, *J. Energy Storage*, 2024, **101**, 113733.

2 K. Mazloomi and C. Gomes, *Renewable Sustainable Energy Rev.*, 2012, **16**, 3024–3033.

3 Q. Wang and K. Domen, *Chem. Rev.*, 2020, **120**, 919–985.

4 T. Hisatomi and K. Domen, *Next Energy*, 2023, **1**, 100006.

5 T. Takata, J. Jiang, Y. Sakata, M. Nakabayashi, N. Shibata, V. Nandal, K. Seki, T. Hisatomi and K. Domen, *Nature*, 2020, **581**, 411–414.

6 M. Kazuhiko and D. Kazunari, *J. Phys. Chem. Lett.*, 2010, **1**, 2655–2661.

7 T. Kawawaki, M. Kawachi, D. Yazaki, Y. Akinaga, D. Hirayama and Y. Negishi, *Nanomaterials*, 2022, **12**, 344.

8 D. Kato, H. Suzuki, R. Abe and H. Kageyama, *Chem. Sci.*, 2024, **15**, 11719–11736.

9 K. Chen, J. Xiao, T. Hisatomi and K. Domen, *Chem. Sci.*, 2023, **14**, 9248–9257.

10 Z. Wang, Y. Inoue, T. Hisatomi, R. Ishikawa, Q. Wang, T. Takata, S. Chen, N. Shibata, Y. Ikuhara and K. Domen, *Nat. Catal.*, 2018, **1**, 756–763.

11 K. Chen, J. Xiao, J. J. M. Vequizo, T. Hisatomi, Y. Ma, M. Nakabayashi, T. Takata, A. Yamakata, N. Shibata and K. Domen, *J. Am. Chem. Soc.*, 2023, **145**, 3839–3843.

12 H. Li, J. Xiao, J. J. M. Vequizo, T. Hisatomi, M. Nakabayashi, Z. Pan, N. Shibata, A. Yamakata, T. Takata and K. Domen, *ACS Catal.*, 2022, **12**, 10179–10185.

13 Q. Wang, M. Nakabayashi, T. Hisatomi, S. Sun, S. Akiyama, Z. Wang, Z. Pan, X. Xiao, T. Watanabe, T. Yamada, N. Shibata, T. Takata and K. Domen, *Nat. Mater.*, 2019, **18**, 827–832.

14 J. Yu, L. Shi, R. Li, J. Huang, R. Wang, Z. Li, C. Shen, G. Liu, Y. Li and X. Xu, *ACS Catal.*, 2024, **14**, 608–618.

15 R. Wang, H. He, L. Shi, D. Du, G. Lin, C. Zhang and X. Xu, *Adv. Energy Mater.*, 2023, **14**, 2302996.

16 A. Kasahara, K. Nukumizu, G. Hitoki, T. Takata, J. N. Kondo, M. Hara, H. Kobayashi and K. Domen, *J. Phys. Chem. A*, 2002, **106**, 6750–6753.

17 F. Zhang, A. Yamakata, K. Maeda, Y. Moriya, T. Takata, J. Kubota, K. Teshima, S. Oishi and K. Domen, *J. Am. Chem. Soc.*, 2012, **134**, 8348–8351.

18 K. Kawashima, M. Hojamberdiev, H. Wagata, K. Yubuta, J. J. M. Vequizo, A. Yamakata, S. Oishi, K. Domen and K. Teshima, *J. Phys. Chem. C*, 2015, **119**, 15896–15904.

19 V. Werner, G. A. Zickler and S. Pokrant, *Prog. Solid State Chem.*, 2024, **73**, 100442.

20 D. Chen, D. Habu, Y. Masubuchi, S. Torii, T. Kamiyama and S. Kikkawa, *Solid State Sci.*, 2016, **54**, 2–6.

21 H. Zhang, Y. Li, Q. Zhang and H. Wang, *Mater. Lett.*, 2008, **62**, 2729–2732.

22 A. E. Maegli, E. H. Otal, T. Hisatomi, S. Yoon, C. M. Leroy, N. Schäuble, Y. Lu, M. Grätzel and A. Weidenkaff, *Energy Procedia*, 2012, **22**, 61–66.

23 A. E. Maegli, S. Pokrant, T. Hisatomi, M. Trottmann, K. Domen and A. Weidenkaff, *J. Phys. Chem. C*, 2014, **118**, 16344–16351.

24 H. Wagata, N. Zettsu, A. Yamaguchi, H. Nishikiori, K. Yubuta, S. Oishi and K. Teshima, *Cryst. Growth Des.*, 2015, **15**, 124–128.

25 K. Kawashima, M. Hojamberdiev, H. Wagata, M. Nakayama, K. Yubut, S. Oishi, K. Domen and K. Teshima, *Catal. Sci. Technol.*, 2016, **6**, 5389–5396.

26 G. Lin and X. Xu, *ACS Sustainable Chem. Eng.*, 2020, **8**, 9641–9649.

27 Y. Li, F. Li, X. Li, H. Song, Z. Lou, Z. Ye and L. Zhu, *Nano Energy*, 2016, **19**, 437–445.

28 G. Lin, X. Sun and X. Xu, *Appl. Catal., B*, 2023, **324**, 122258.

29 M. Matsukawa, R. Ishikawa, T. Hisatomi, Y. Moriya, N. Shibata, J. Kubota, Y. Ikuhara and K. Domen, *Nano Lett.*, 2014, **14**, 1038–1041.

30 J. Song, Y. Lu, Y. Lin, Q. Liu, X. Wang and W. Su, *Appl. Catal., B*, 2021, **292**, 120185.

31 M. Inose, S. Nakakura, T. Hisatomi, T. Takata and K. Domen, *Adv. Energy Sustainability Res.*, 2024, 2400321.

32 M. A. A. Júnior, M. I. B. Bernardi and A. Mesquita, *J. Alloys Compd.*, 2023, **955**, 170147.

33 A. B. Posadas, C. Lin, A. A. Demkov and S. Zollner, *Appl. Phys. Lett.*, 2013, **103**, 142906.

34 Y. Masuda, R. Mishima, M. Yamada, H. Ando, T. Kawasaki, K. Murai and T. Moriga, *IOP Conf. Ser.: Mater. Sci. Eng.*, 2009, **1**, 012018.

35 F. Wu, G. Liu and X. Xu, *J. Catal.*, 2017, **346**, 10–20.

36 X. Sun, Y. Mi, F. Jiao and X. Xu, *ACS Catal.*, 2018, **8**, 3209–3221.

37 A. E. Maegli, E. H. Otal, E. T. Hisatomi, S. Yoon, C. M. Leroy, N. Schäuble, Y. Lu, M. Grätzel and A. Weidenkaff, *Energy Procedia*, 2012, **22**, 61–66.

38 L. Lu, B. Wang, S. Wang, Z. Shi, S. Yan and Z. Zou, *Adv. Funct. Mater.*, 2017, **27**, 1702447.

39 S. Pokrant, M. C. Cheynet, S. Irsen, A. E. Maegli and R. Erni, *J. Phys. Chem. C*, 2014, **118**, 20940–20947.

40 Y. Li, X. Cheng, X. Ruan, H. Song, Z. Lou, Z. Ye and L. Zhu, *Nano Energy*, 2015, **12**, 775–784.